Biophysical Journal
Article

Biophysical Society

Dynamics of the HIV Gag Lattice Detected by Localization Correlation Analysis and Time-Lapse iPALM

Ipsita Saha[1,2] and Saveez Saffarian[1,2,3,*]
[1]Center for Cell and Genome Science, [2]Department of Physics and Astronomy, and [3]Department of Biology, University of Utah, Salt Lake City, Utah

ABSTRACT Immature human immunodeficiency virus (HIV) virions have a lattice of Gag and Gag-Pol proteins anchored to the lumen of their envelope. Using electron microscopy, we demonstrate that HIV virus-like particles (VLPs) assembled by the viral protein Gag and tagged at its C-terminus with the fluorescent protein Dendra2 have the same morphology and size as the VLPs assembled using only HIV Gag. We characterize the photophysical properties of Dendra2 and demonstrate that 60% of Dendra2 molecules can be photoswitched and reliably counted in our interferometric photoactivated localization microscopy (iPALM) setup. We further perform iPALM imaging on immobilized HIV Gag-Dendra2 VLPs and demonstrate that we can localize and count 900–1600 Dendra2 molecules within each immobilized VLP with a single-molecule localization precision better than (10 nm)^3. Our molecular counts correspond to 1400–2400 Gag-Dendra2 proteins incorporated within each VLP. We further calculate temporal correlation functions of localization data, which we present as localization correlation analysis, and show dynamics within the lattice of immobilized VLPs in the timescale of 10–100 s. We further use our localization data to reconstruct time-lapse iPALM images of the Gag-Dendra2 lattice within the lumen of immobilized VLPs. The iPALM time-lapse images show significant lattice dynamics within the lumen of VLPs. Addition of disuccinimidyl suberate to the VLPs completely abrogated these dynamics as observed in both localization correlation analysis and time-lapse iPALM. In a complementary approach, we utilized HaXS8 cross-linking reactions between Halo and SNAP proteins and verified lattice dynamics in purified VLPs incorporating 10% Gag-SNAP, 10% Gag-Halo, and 80% Gag proteins. The HIV Gag lattice, along with the structural lattice of other enveloped viruses, has been mostly considered static. Our study provides an important tool to investigate the dynamics within these enveloped viruses.

SIGNIFICANCE HIV Gag lattice, along with the structural lattices of many other viruses, has been mostly considered static. Our study provides an important tool to investigate the dynamics within these lattices.

INTRODUCTION

The immature lattice of Gag within human immunodeficiency virus (HIV) virions is easily visualized in negative-stain thin-section electron microscopy. Based on close-packing symmetrical calculations and mass of viral components, it was estimated that immature HIV virions should incorporate as many as ~5000 Gag molecules (1,2). Quantification of total fluorescence from individual virus-like particles (VLPs) using a photon-counting histogram (PCH), however, showed a much lower number of Gag molecules within individual VLPs (3). The holes and imperfections that correspond to the lower-than-5000 copies of Gag proteins incorporated within each VLP were then directly observed by electron cryotomography of released HIV virions and budding sites (4–6). Why such defects exist within the lattice of HIV and whether they have a functional role is largely unknown (4,7). Expression of HIV Gag protein by itself is sufficient to drive the formation of VLPs with similar morphology to HIV virions (8).

After release from the infected cells, HIV virions undergo maturation that transforms them into infectious particles. HIV maturation is catalyzed by the 22 kDa HIV protease homodimer. The homodimer is assembled from the 11 kDa protease domain embedded within the Gag-Pol polyprotein. In a series of proteolytic events, the 22 kDa protease

Submitted January 3, 2020, and accepted for publication June 2, 2020.
*Correspondence: saffarian@physics.utah.edu
Editor: Julie Biteen.
https://doi.org/10.1016/j.bpj.2020.06.023

homodimer forms and releases all domains within Gag and Gag-Pol polyproteins (9). Delay in the release of the immature virus results in premature protease activation and release of noninfectious particles (10). The proteolysis is essential for the formation of the conical capsid structure, which encapsulates the viral genome and genome enzymes (11). The mechanism by which the protease domain embedded within the Gag-Pol polyprotein gets activated is not well understood. It is also unclear whether the architecture of the immature lattice plays any role in the release of the 11 kDa protease from its confinement within the Gag-Pol polyprotein.

It is now estimated, based on cryotomography data, that immature HIV virions incorporate ~2000 copies of Gag and ~100 copies of Gag-Pol within the immature HIV lattice anchored to the lumen of the ~140 nm diameter viral envelope (4,7). Although PCH methods can be used to quantify the fluorescence intensity in moving objects (12,13), quantifying protein copy numbers within stationary biological structures using optical microscopy is nontrivial. Information about the stoichiometry of proteins within structures can be extracted from the intensity measurement of the fluorescent proteins that are used to tag the proteins of interest (14,15). TIRF microscopy has proved to be an efficient method of quantifying membrane-bound proteins by exploring the discrete photobleaching behavior of the green fluorescent proteins (16). Yellow fluorescent proteins have also been used for quantification of a wide range of protein copy numbers within cells (17). However, the introduction of photoactivated localization microscopy not only increased the localization precision but also took advantage of the stochastic behavior of the photoactivatable fluorescent proteins to quantify their copy numbers by temporal separation (18). Developments in counting single molecules accounting for their blinking behavior ranged from semiempirical approaches (19) to the more systematic ones (20,21). These methods have been applied to count proteins both within large as well as small structures, as reviewed in (22).

Localization microscopy can also significantly increase the resolution of optical imaging and explore the structural organization of macromolecular structures (23–25). Although in first applications, localization microscopy was limited to improving the resolution only within the plane of focus to below 10 nm, the introduction of multiphase interferometry within localization microscopy (iPALM) has improved the resolution along the optical axis, resulting in homogeneous voxel sizes below $(10\ \text{nm})^3$ (26). When the samples are not fixed, localization microscopy inherently harbors data about the dynamics of the system as the structures undergo dynamics during data acquisition. Analysis of these dynamics with localization microscopy has previously been used to measure high-resolution dynamics in cellular environments (27–30). Single-molecule localization microscopy has also been used to monitor VLP assembly (31) and to visualize the relationship between cellular components, specifically ESCRTs and HIV Gag VLPs (32–34).

We have previously imaged purified HIV Gag-Dendra2 VLPs using correlative iPALM and scanning electron microscopy (SEM) and visualized the virion cavity as well as defects within the immature Gag lattice (35). Although these observations are at a much lower resolution compared to electron cryotomography, iPALM resolves the HIV Gag lattice at ambient temperature within an aqueous environment. In this study, we demonstrate how all Gag-Dendra2 molecules incorporated within the VLPs can be accounted for and how the temporal acquisition of iPALM data can be used to visualize dynamics within the HIV Gag-Dendra2 lattice within the immobilized VLPs. We also present evidence of dynamics within the HIV Gag lattice using VLPs incorporating 10% Gag-SNAP, 10% Gag-Halo, and 80% Gag. We used HaXS8 to dimerize SNAP and Halo in vitro. Our biochemical data supports the existence of multi-timescale dynamics within the Gag lattice of purified VLPs.

MATERIALS AND METHODS

Design of Dendra2 tandems for photophysical characterization

Dendra2 was obtained from Addgene (Watertown, MA). We designed Dendra2 tandem chains of one, two, and three Dendra2 molecules. To help immobilize these molecules on glass coverslips for imaging and counting purposes, we inserted an engineered monomeric streptavidin protein (mAvidin), previously described (36), at the N-terminus of each tandem chain. The Dendra2 and mAvidin proteins were further separated by insertion of a glycine-rich linker sequence (flex: GGGGSGGGGSGGGGSGGGGD). This resulted in three separate tandems:

Tandem (1): mAvidin-Flex-Dendra2,
Tandem (2): mAvidin-Flex-Dendra2-Flex-Dendra2, and
Tandem (3): mAvidin-Flex-Dendra2-Flex-Dendra2-Flex-Dendra2.

The Dendra2 tandem chains were encoded into the mammalian expression plasmid pCDNA3.1 (sequence files available in Supporting Materials and Methods). The plasmids were then transfected into the 293T cells. 36 h post-transfection, cells were collected and lysed using NP40-based lysis buffer (containing 1% NP40 detergent, 150 mM NaCl, and 50 mM tris-HCL (pH 8.0)). The cell lysates were further sonicated using a probe sonicator (fisherband, Pittsburgh, PA). The supernatant, which contained the tandem Dendra2 molecules, was separated from the cell debris through centrifugation at 15,000 rpm for 15 min.

Sample preparation and imaging of the Dendra2 tandem chains

30 μL (diluted from the stock in PBS in the ratio 1:3) of the Dendra2 Tandems, as described above, were sandwiched between a 25 mm #1.5 Hestzig coverslip (from Hestzig, Leesburg, VA) and an 18 mm #1.5 coverslip (fisherbrand). The coverslips were first immersed in 1 M NaOH solution for an hour, followed by MilliQ water for another hour. They were then blow-dried with nitrogen and ozone cleaned (Novascan UV Ozone Cleaner; Novascan, Ames, IA) for 1 h with an oxygen flow of 1 L per min. 40 μL of PPL-g-PEG (from SuSoS Surface Technology, Dubendorf, Switzerland) at a

concentration of 1 mg/mL was added to the 25-mm coverslip immediately and incubated at room temperature in a humid environment. After the incubation period, the coverslip was thoroughly washed with MilliQ water and blow-dried with nitrogen.

To make the sandwich samples 30 μL of the supernatant containing Dendra2 tandem single molecules were added to glass coverslips prepared as described above and incubated for 15 min. Then, the coverslip was gently washed with PBS so as to remove the molecules that did not adhere to the coverslip. The excess quantity of PBS was maintained on the 25-mm Hestzig coverslip, sandwiched with the 18 mm coverslip, and sealed with glue (ClearWeld; J-B Weld, Sulphur Springs, TX).

The sandwiched samples of single molecules were imaged immediately after preparation. The sample is positioned onto the micro-positioning stage and illuminated by a 315 mW of 561 nm laser. A Nikon 60× Apo TIRF objective was used to focus on the 100 nm gold fiducials that are embedded in the 25 mm Hestzig coverslips. Pseudo-TIRF conditions were maintained by directing the laser into the sample so as to increase the signal/noise ratio from the single molecules. The experiment was performed on the prototype setup by Thermo Fisher Scientific (Waltham, MA), which is equipped to perform iPALM experiments as previously described (35,37). Fluorescence signal from the sample was detected by a Hamamatsu (Hamamatsu City, Japan) ORCA-Flash 4.0 sCMOS camera. Data were collected for 15,000 frames with 100 ms exposure of a 561 nm laser, and the single molecules were activated by a 405 nm laser every 10 frames, with a constant activation scheme of 100 ms. The same imaging conditions were maintained for imaging Tandem (1), Tandem (2), and Tandem (3) molecules. We observed that the mAvidin molecules would dissociate from the PPL-g-PEG-coated coverslip after 2 h of the initial binding (half-life ~2 h); therefore, the experiments were performed within 1 h of the initial binding.

Sample preparation and imaging of the Gag-Dendra2 VLPs

The Gag-Dendra2 VLPs were harvested from 293T cells. The VLPs were segregated from the cell supernatant by centrifugation through 10% sucrose gradient at 10,000 × g for 2 h in Beckman L8-70M Ultracentrifuge and SW41 rotor (Beckman Coulter, Brea, CA). The VLP pellet was then resuspended in PBS. For iPALM imaging, the sample was sandwiched between a 25 mm #1 Hestzig and 18 mm #1.5 coverslips. The coverslips were first immersed in 1 M NaOH solution for an hour and then in MilliQ water for another hour. They were then blow-dried with nitrogen. They were then cleaned in ozone for an hour with an oxygen flow of 1 L per min. The 25 mm Hestzig coverslip was then coated with poly-D-lysine from Sigma-Aldrich (St. Louis, MO) at a concentration of 50 μg/ml and incubated in a humid atmosphere for 45 min. After the incubation period, the coverslip was thoroughly washed with mQ water and blow-dried with nitrogen. The VLPs were immediately added to the dried coverslip and incubated for 30 min. The coverslip was washed gently with PBS to remove the VLPs that have not immobilized. Care was taken so as not to dry the coverslip after being washed with PBS. This 25 mm Hestzig was then sandwiched with the 18-mm coverslip and sealed with glue (ClearWeld quick setting epoxy by J-B Weld) before imaging. For fixation of the VLPs, a stock solution of 25 mM disuccinimidyl suberate (DSS) (abcam, Cambridge, United Kingdom) was freshly prepared and added to the VLPs to a final concentration of 5 mM and incubated at room temperature for 30 min. Then, a quench solution (1 M Tris (pH 7.5)) was added to a final concentration of 25 mM to quench the reaction and incubated at room temperature for 1 h before the fixed VLPs were immobilized on the 25 mm Hestzig coverslip with the same protocol outlined above.

The time-lapse iPALM measurements of the VLPs were performed on a prototype setup by Thermo Fisher Scientific. The sandwiched sample was secured onto a micro-positioning stage and illuminated by a 315 mW 561 nm laser. Two Nikon 60× Apo TIRF objectives focused on the sample from top and bottom. The custom three-way beam splitter was adjusted so as to get the interference and maintain a 120° phase shift between the cameras (ORCA-Flash 4.0 sCMOS; Hamamatsu). The system was calibrated using the gold fiducials embedded in the 25 mm Hestzig coverslip so as to obtain a localization precision of $\sigma \leq 10$ nm in both the axial as well as the optical direction. The 561 nm laser used to illuminate the sample was directed well into the sample, so instead of maintaining a TIRF condition, a pseudo-TIRF condition was maintained. This helped to get a better signal from the entire VLP. For the first set of images, 5000 frames were acquired with 100 ms of exposure of the 561 nm laser, and the Dendra2 molecules were photoactivated using 405 nm laser with an exposure of 10 ms every 10 frames. After a time-lapse of 10 min, the second set of 5000 frames was acquired with 100 ms exposure of the 561 nm laser, and the 405 nm laser was shot with an exposure of 100 ms every 10 frames. To bleed out the maximal number of molecules, a third set of 5000 frames was acquired after a time-lapse of 10 min with a 100 ms exposure of 561 nm and a 300 ms exposure of 405 nm laser every 10 frames. Identical imaging conditions were maintained for both fixed and nonfixed VLPs.

TEM sample preparation and imaging

U2OS cells were grown on ACLAR disks and transfected with either Gag or Gag-Dendra2 plasmids (Dendra2 is inserted at the C-termini of the Gag-p6, sequences provided in the Supporting Materials and Methods). Cells were fixed in 2.5% glutaraldehyde plus 1% paraformaldehyde in 0.1 M cacodylic buffer for 30 min and then embedded in resin using an EMbed 812 Kit (Electron Microscopy Sciences, Hatfield, PA) and sectioned at 80 nm with a diamond knife (Diatome, Nidau, Switzerland) using a Leica EM UC6 (Leica Microsystems, Wetzlar, Germany). Sections were visualized using a JEM1400-Plus Transmission Electron Microscope (JEOL, Tokyo, Japan) at 120 kV.

Sample preparation for in vitro biochemical analysis

293T cells were grown in full DMEM medium supplemented with 10% FBS. Cells were co-transfected with 80% of Gag, 10% of Gag-SNAP, and 10% of Gag-Halo plasmids (sequences provided in the Supporting Materials and Methods). Both SNAP and Halo were tagged at the C-terminus of Gag, similar to Gag-Dendra2. 36 h post-transfection, the VLPs were harvested with the same protocol used for purifying Gag-Dendra2 VLPs. For the biochemical analysis, these VLPs were treated with HaXS8 dimerizer (from Tocris Biosciences, Bristol, United Kingdom) at the indicated concentration and incubated at 37°C for ~10 min. They were then denatured by Laemmli sample buffer (Bio-Rad Laboratories, Hercules, CA) with 5% BME and boiled at 95°C for 10 min. The proteins were separated by SDS-PAGE and then transferred to a PVDF membrane (Millipore, Burlington, MA). Membranes were stained with anti-HIV-1 p24 monoclonal (183-H12-5C; National Institutes of Health, AIDS Reagent Program, National Institutes of Health, Bethesda, MD) primary antibody and then immunoprobed with appropriate infrared anti-mouse secondary antibody. The membrane was scanned with the Odyssey Infrared Imaging System (LI-COR Biosciences, Lincoln, NE) according to the manufacturer's manual instruction at 700 nm. For the biochemical analysis, the VLPs were treated with HaXS8 at 1 μM and incubated at 37°C for the indicated amount of time and then denatured the same way as indicated above. The amount of proteins in each band was quantified by cumulative intensity analysis using ImageJ software.

Transfection protocol

All 293T cells were grown in DMEM supplemented with 10% FBS at 37°C. All plasmids were transfected using Lipofectamine 2000 (Thermo Fisher Scientific).

RESULTS

Quantification of Dendra2 photophysics

Dendra2 is a fluorescent protein genetically modified to photoswitch upon exposure to 405 nm excitation from emitting green fluorescence to red (38). The low-blinking-rate characteristics of Dendra2 is advantageous for molecular counting applications (20,21). Before using Dendra2 fused to Gag, we characterized Dendra2 to find out how many Dendra2 molecules we can practically photoswitch and count in our iPALM setup.

To quantify the photophysical behavior of Dendra2 molecules, we designed three Dendra2 tandem chains that would elucidate not only the blinking and photobleaching but also the proximity-quenching effects of the Dendra2 molecules. Dendra2 tandem protein chains have either one Dendra2 (Tandem (1)), two Dendra2 (Tandem (2)), or three Dendra2 (Tandem (3)) molecules, as described in Materials and Methods. To help immobilize the Dendra2 tandem chains, we added an engineered monomeric mAvidin protein at the N-terminus of each tandem chain and anchored the chains onto glass coverslips covered with PEG/PEG-biotin as outlined in Materials and Methods. Tandem (3), in particular, was designed to probe the effects of close proximity on Dendra2 photophysics.

Imaging of Dendra2 molecules and their molecular counting is well established (20,21,35). For brevity, we used a pseudo-TIRF excitation module as described in Materials and Methods and exposure time of 100 ms. Under these conditions, most Dendra2 molecules were photobleached within one to two frames. Similar to the counting schemes suggested before (20), we attributed the signal from molecules appearing within a time window of τ_c as emanating from the same molecule undergoing blinking.

Fig. 1 summarizes both raw data as well as counting statistics from Tandem (1)-, Tandem (2)-, and Tandem (3)-immobilized molecules on glass coverslips. Tandem (1) data shows that under the scheme of our activation, 67% of single Dendra2 molecules photobleached after activation within a single frame. The single molecules that did not photobleach within one frame were registered in one or two more additional frames. As shown in Fig. 1, when a $\tau_c = 1$ s (10

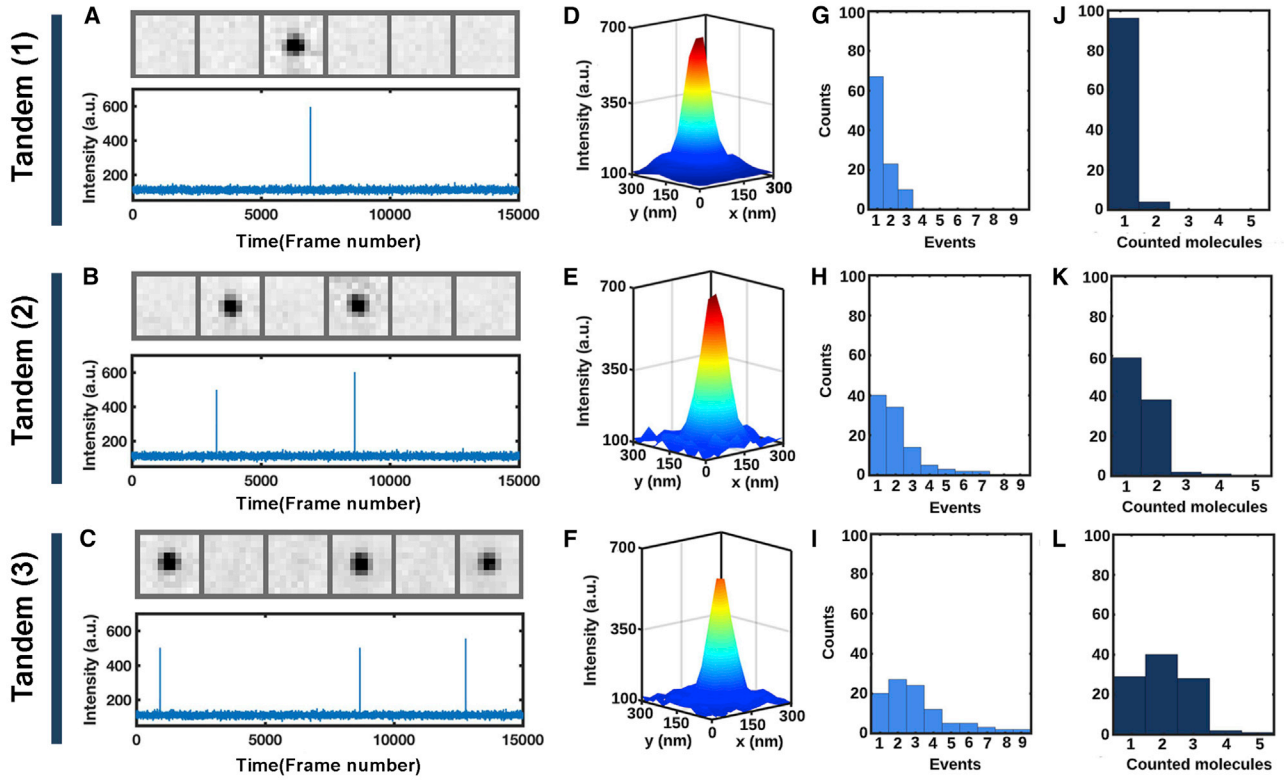

FIGURE 1 Photophysical characterization of Dendra2 tandem chains immobilized on glass coverslips. (*A*)–(*C*) show the time trace of Dendra2 photoactivation and bleaching for (*A*) Tandem (1), which has a single Dendra2 molecule; (*B*) Tandem (2), which has two Dendra2 molecules; and (*C*) Tandem (3), which has three Dendra2 molecules. (*D*)–(*F*) show the PSF of the activated Dendra2 molecules in (*D*) Tandem (1), (*E*) Tandem (2), and (*F*) Tandem (3). (*G*)–(*I*) show histograms of the number of frames in which Dendra2 molecules were detected from (*G*) Tandem (1) molecules, (*H*) Tandem (2) molecules, and (*I*) Tandem (3) molecules. (*J*)–(*L*) show the number of molecules counted in the same data set as (*G*)–(*I*) with optimized τ_c. The number of molecules counted is lower than the number of frames in which molecules were detected because all Dendra2 molecules appearing within the $\tau_c = 10$ frame window were considered to be from a single molecule. To see this figure in color, go online.

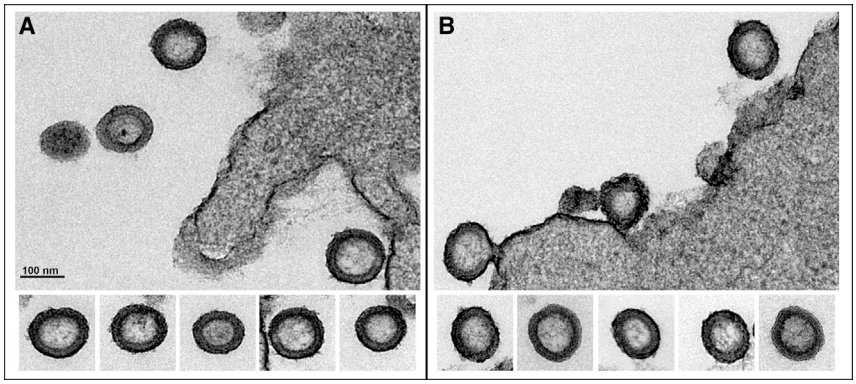

FIGURE 2 TEM images of VLPs in the process of releasing from U2OS cells. Images show 80 nm sections of negative-stain TEM of U2OS cells transfected with 100% HIV Gag wild-type (WT) (*A*) and U2OS cells transfected with 100% Gag-Dendra2 (*B*). Five representative VLPs of each kind are shown at the bottom of each panel.

frames) was used, we were able to count 95% of events in Tandem (1) as individual molecules of Dendra2.

It is not possible to find the percentage of Dendra2 molecules that can be photoswitched from the analysis of Tandem (1) data. In contrast, Tandem (2) and Tandem (3) data inherently show the probability of photoswitching a single Dendra2 molecule. Based on data presented in Fig. 1 from Tandem (2) and Tandem (3), we estimate that each Dendra2 molecule has an independent probability of detection that is approximately 60%. Furthermore, activation of the Dendra2 was seen to be completely stochastic, and there was no sign of quenching when the molecules were in close proximity as would be the case when they are attached by flex linkers in Tandem (2) and Tandem (3).

We further utilized the single-molecule data collected from Tandem Dendra2 experiments to establish the localization precision of our iPALM setup. As shown in Fig. S1, the molecules were all localized with a precision in excess of $(10\ \text{nm})^3$.

Electron microscopy on Gag-Dendra2 VLPs

Fluorescently tagged Gag VLPs have been previously shown to have similar morphology to wild-type (WT) Gag VLPs (3). We have also previously immobilized Gag-Dendra2 VLPs on glass coverslips and imaged them using correlative iPALM and SEM (35); however, the SEM is a surface electron microscopy imaging technique and would not be sensitive to subtle differences in morphology of the lattice between Gag WT and Gag-Dendra2 VLPs. To further analyze the morphology of the released Gag-Dendra2 VLPs and compare them to Gag VLPs, we imaged U2OS cells in the process of releasing VLPs by fixing the cells, embedding them in resin, cutting 80 nm sections, and imaging them with negative-stain EM. Thin-section electron micrographs for the above conditions are shown in Fig. 2. Samples were prepared by transfecting U2OS cells with (Fig. 2 *A*) 100% Gag WT and (Fig. 2 *B*) 100% Gag-Dendra2.

Analysis of the electron micrographs did not reveal any difference between VLPs assembled from Gag versus Gag-Dendra2. The measured size distribution was 150 ± 15 nm in WT and 155 ± 20 nm in Gag-Dendra2 VLPs. Additional electron micrographs of virions with 20% Gag-Dendra2 plus 80% Gag WT and 80% Gag-Dendra2 plus 20% Gag WT are shown in Fig. S2.

Imaging and counting Gag-Dendra2 molecules within immobilized VLPs using iPALM

Not detecting any morphological difference between Gag and Gag-Dendra2 VLPs, we proceeded to exclusively image the Gag-Dendra2 VLPs (with 100% of molecules tagged with Dendra-2) with iPALM. Gag-Dendra2 VLPs harvested from 293T cells were immobilized on glass coverslips using nonspecific interactions and imaged with iPALM microscopy as described in Materials and Methods. We specifically designed these experiments to photoswitch the maximal number of Dendra2 molecules within each VLP. The exposure time for the 561 nm laser was set at 100 ms, which, according to our characterization from Dendra2 as presented in Fig. 1, is sufficient to photobleach most of the photoswitched molecules in one frame. This exposure also results in the acquisition of enough photons to localize the Dendra2 molecules within 6 nm in the axial plane and 3 nm along the optical axis (Fig. S1). The exposure of 405 nm laser was subsequently increased during the three sets of images as described in Materials and Methods.

The experiment was performed in three imaging sets, each with 5000 frames with a 10 min delay between the sets. VLPs that were located within proximity of at least three fiducial gold particles were chosen for analysis. The vicinity of gold fiducials embedded in the 25 mm Hestzig slides guaranteed continuity of local drift correction through the full three sets of 5000 frames.

In total, 100 VLPs were analyzed. We report counting, on average, 1200 individual Dendra2 with a range from 900 to 1400 within individual immobilized Gag-Dendra2 VLPs (Fig. S3). Not all Dendra2 molecules can be counted in our setup, as shown in Fig. 1. Characterization of Dendra2, as presented in the above section, gives a 60% probability of counting Dendra2 molecules in our setup. These corrections

would yield an average of 2000 Gag-Dendra2 molecules with a range from 1400 to 2400 incorporated within individual immobilized Gag-Dendra2 VLPs. The localization precision for the Dendra2 molecules within the VLPs was 6 and 5 nm in the axial plane and 3 nm in the optical axis (Fig. S1).

Fig. 3 demonstrates the localizations within a 16 nm slice at the center of the VLP. The Dendra2 localizations show a void space at the center of the VLP and inhomogeneity within the lattice. The slice incorporates data from all 15,000 frames. The distance histogram in Fig. 3 *D* indicates the radial range of the localizations of the Dendra2 molecules. These localizations peak at 20–40 nm from the center of the VLP and are consistent with the position of Dendra2 at the C-terminus of Gag.

Localization correlation analysis

The localization data from each individual VLP, as presented in the previous section, are the three-dimensional (3D) coordinates of Dendra2 molecules activated randomly during a period of ~1.5 h. Each 3D localization is measured in a specific time, clocked by the frame number in which the molecule was measured. It is to be noted that the dead frames due to the exposure of the 405 nm laser have been taken into consideration when reconstructing the real-time localization pulse of a VLP from all the three sets of images. Therefore, the 3D localization of molecules can be coded by the following vector:

$$L_i(t : x, y, z),$$

in which i is the molecule number, t is the measured time as frame number, and x, y, and z are the localization values for the molecule. L is a direct function of t; L = 1 at the time point t, at which the molecule was localized, and L = 0 at any other point.

To quantify the number of localizations within any given volume (v) of the VLP at any given moment (t), we define

$$VLP_v(t) = \sum_{i=1}^{N} L_i(t : ((x, y, z) \mid v)).$$

The sum is carried on L_i, where x,y,z belongs to the volume v. $VLP_v(t)$ is basically the number of molecules localized within a subvolume (v) at any given time point (t).

To quantify the persistence of localizations registered at any volume v within the VLP, one can calculate the localization temporal correlation function as defined below:

$$G(\tau_n) = \frac{\langle VLP_v(t+\tau_n) \times VLP_v(t) \rangle}{\langle VLP_v(t)^2 \rangle}.$$

The incorporation of $G(\tau_n)$ in terms of multi-τ correlation algorithm and its normalization has been outlined in detail in the Supporting Materials and Methods. It is of note that $G(\tau_n)$ is only meaningful at τ-values larger than the exposure time and measures the persistence of the structure at volume v over time. In the ideal case, if there are an infinite number of single molecules that can be photoswitched randomly within a fixed structure, $G(\tau_n)$ would faithfully represent the structural persistence within the system. However, in the laboratory case, the number of single molecules within the structure is limited, and therefore, even in a fixed structure, one would expect that $G(\tau_n)$ would decay at the timescale at which all single molecules have been bleached within the structure.

We aligned the VLPs and sectioned them uniformly into eight segments, as indicated in the inset of Fig. 4, *A* and *B*. The time pulses from each segment were analyzed using a multi-τ correlation algorithm implemented on $G(\tau_n)$ (as detailed in the Supporting Materials and Methods). Two representative time pulse signals from a section of each

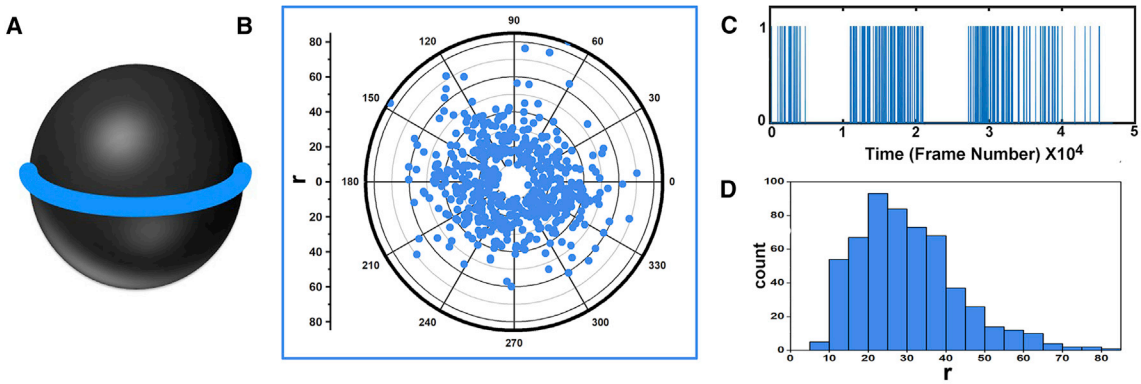

FIGURE 3 Visualization of Gag-Dendra2 molecules within a 160 nm slice of the Gag-Dendra2VLP. (*A*) Model of a VLP depicted as a black sphere with a diameter of 150 nm. The blue line represents the location of the 16 nm slice within which all localized Dendra2 molecules were plotted; the slice was exactly around the center of mass of the VLP. (*B*) Polar plot of the Dendra2 molecules within the slice identified in (*A*). (*C*) Time trace of Dendra2 molecules localized within the 16 nm slice shown in (*A*) and plotted in (*B*). The time-trace registers a value of 1 in the frame when a molecule was localized and a value of 0 otherwise. (*D*) The distribution of the radial distance of Dendra2 molecules with respect to the center of the VLP within the indicated slice. To see this figure in color, go online.

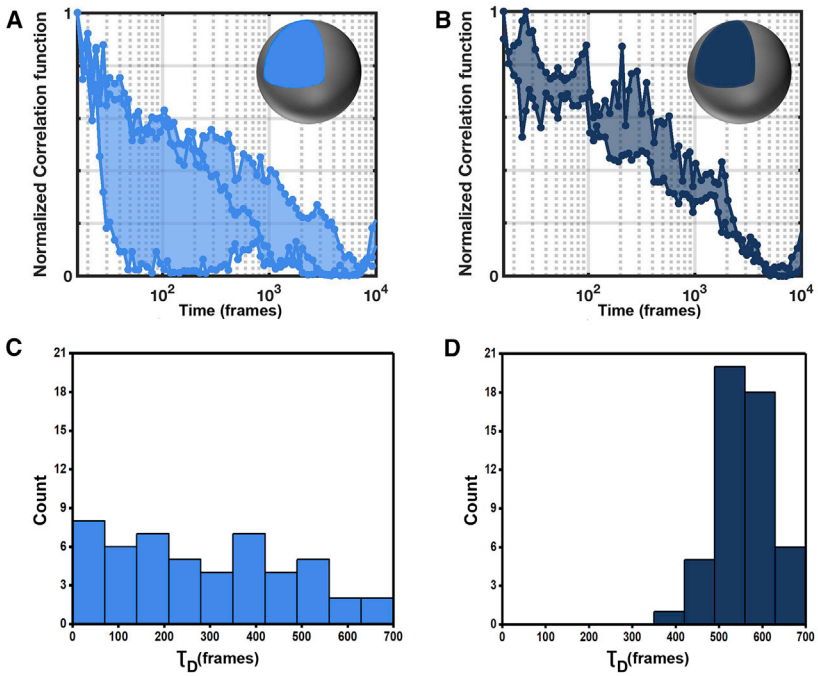

FIGURE 4 Localization correlation function analysis for the Gag-Dendra2 VLPs. (*A*) shows three representative localization correlation functions, each calculated from a separate VLP from similar sections as identified in the inset of (*A*). The shaded area in the correlation function shows the variation of the decay of the correlation functions from 50 VLPs. (*C*) represents the range of the τ_D as calculated by fitting the correlation functions from all the sections of the 50 VLPs. (*B*) and (*D*) are identical to (*A*) and (*C*), except the Gag-Dendra2 VLPs in this case were treated with DSS as outlined in the text. To see this figure in color, go online.

VLP (one for the WT and the other treated with DSS) have been shown in Fig. S6.

50 VLPs, which had eight sections each, were analyzed. As shown in Fig. 4, the localization correlation analysis (LCA) shows a range of decays in which all the segments from the 50 VLPs were considered. To avoid any possible source of bias, only volumes with a similar total number of molecules localized were used for LCA. As explained above, the LCA correlation functions decay because of structural dynamics as well as eventual photobleaching effects. To separate the two effects, we treated the VLPs with a membrane-permeable fixative, DSS, and analyzed 50 fixed VLPs in the same manner. Fig. 4 also summarizes the effect of the fixative on the VLPs. The correlation functions analyzed over a range of 50 fixed VLPs showed only decay times in excess of 1000 frames. Representative galleries of correlation functions from Gag-Dendra2 VLPs with and without application of DSS are shown, respectively, in Figs. S4 and S5. The decay timescales in the correlation functions were further analyzed and are presented in Fig. 4.

We conclude that the decay in the correlation functions, as observed in the fixed VLPs, are due to the photobleaching effects of the molecules in the segments. For the nonfixed VLPs, there is decay due to dynamics in addition to photobleaching effects. As shown in Figs. 4 and S4 and S5, not all sections of the VLPs have similar dynamics.

Time-lapse iPALM on the Gag-Dendra2 VLPs

Although the correlation functions that quantify the dynamics within the Gag-Dendra2 lattice show large inhomogeneity within individual VLPs, one would predict that such dynamics should also be detectable using the raw data from the time-lapse iPALM. To further visualize the dynamics, we therefore took slices of the same VLP captured in different time points. To clearly understand the morphology of the lattice, we show localization of all Dendra2 molecules within a 16 nm section at the center of the VLP at two different time points separated by Δt ($\sim$22 $\pm$ 4 min). Fig. 5 shows a 16 nm section of a representative VLP at two different time points (Fig. 5, *A–D*) and another representative VLP with added DSS (Fig. 5, *E–H*). It is important to note that during iPALM imaging each Dendra2 molecule is activated and bleached during its localization; therefore, a molecule that is registered in one time point will not be visualized in the second time point. This makes a direct comparison between sections presented in Fig. 5, *C–F* complicated. To better understand the dynamics, we provide the following statistical analysis of the plots presented in Fig. 5. Let us say that we detect n molecules in a certain section of the VLP at time t and n' molecules in the same section at time $t + \Delta t$. If the localized molecules at time point t correspond to a static structure of Gag, the probability of detecting n′ localizations from the same section at time $t + \Delta t$ will be given by the following: $P = e^{-(n'-n/\sigma)^2}$. In an ideal case, if $n = n'$, then $P = 1$, indicating no change to the underlying lattice (detailed calculation presented in Supporting Materials and Methods). Because of the stochastic activation of the molecules, we expect a high value of P in case of the underlying structure remaining static.

The VLPs in Fig. 5 were divided into eight sections according to r- and θ-values (r from 0 to 40 or

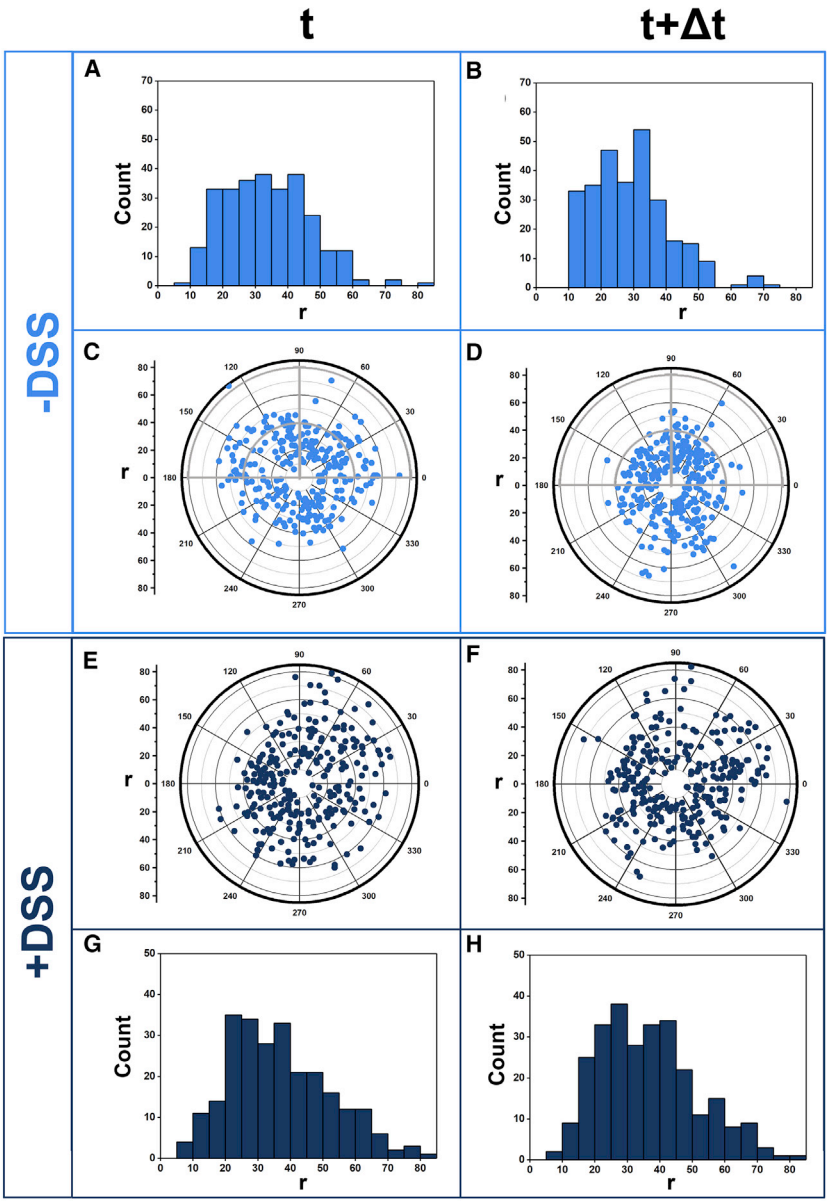

FIGURE 5 Visualization of Gag lattice dynamics from the reconstructed time lapse. Localizations within a 16 nm slice around the center of VLPs are shown from two different time points. (*A*)–(*D*) show the condition for the VLP not treated with DSS. (*A*) and (*B*) show the radial distribution of the localizations within each section for the VLP. (*C*) and (*D*) show the localization of Dendra2 molecules from (*A*) and (*B*) projected into a two-dimensional surface at each time point. (*E*)–(*H*) show the same properties in a VLP treated with the membrane-permeable fixative DSS. Δt represents the time between the acquisition of the images and has a value of ~22 ± 4 min. Sections within the WT VLP with significant morphological changes are highlighted by light gray lines. To see this figure in color, go online.

40–80 nm and θ from 0 to 90, 90–180, 180–270, and 270–360. Section numbers and geometry are shown in the Fig. S7). In the case of the WT VLP as shown in Fig. 5, *A–D*, the *P*-value in all eight sections range from $1.96e^{-13}$ to 0.670 (data for all sections is presented in Supporting Materials and Methods). Specifically, three of the sections in Fig. 5 *C* registered *p*-values below e^{-6}, and one section registered with a *p*-value of e^{-3}. These sections are marked with light gray markings in Fig. 5, *C* and *D*. For the VLP fixed with DSS and shown in Fig. 5, *E–H*, the *p*-value ranged between 0.194 and 1, and no sections were identified with *p*-values below or equal to e^{-3}. This analysis suggests that lattice dynamics within the lattice of the WT VLP is heterogeneous, only affecting certain sections in the observed time, as was also observed with LCA analysis.

Estimate of NC and p6 flexibility on observed dynamics

The CA interactions within the immature lattice of HIV are well characterized by cryotomography (6); however, configurations of NC and p6 within the immature lattice are less well characterized. Our measurements are reporting dynamics observed in Dendra2 molecules positioned after the p6 domain of Gag. We set out to understand how a presumed structural flexibility in NC and p6 can affect our

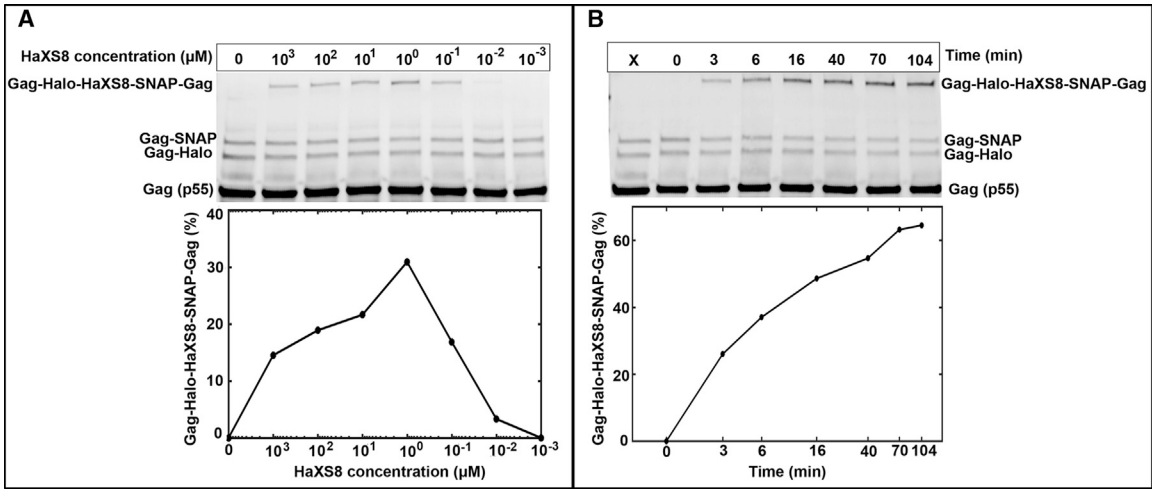

FIGURE 6 Biochemical verification of Gag lattice dynamics. Shown are Western blot analyses of VLPs incorporating 80% Gag, 10% Gag-SNAP, and 10% Gag-Halo. In (*A*), the VLPs were treated with HaXS8 with the indicated concentration and incubated for ~10 min. The graph below the gel indicates the density of SNAP-Halo complex obtained in each case. For a very high or very low amount of HaXS8, the SNAP-Halo complex is low, and it peaks at 1 μM HaXS8. In (*B*), the VLPs were treated with 1 μM HaXS8 and incubated for the indicated amount of time. The graph below the gel in (*B*) indicated the percentage of SNAP-Halo complex obtained for each time. The SNAP-Halo complex increases with increase in time, which supports dynamics within the lattice of HIV Gag VLP.

observed dynamics. A theoretical model was built based on a fully static CA lattice and completely flexible NC and p6 domains, which would allow full rotational dynamics to Dendra2 molecules (details in the Supporting Materials and Methods). In these simulations, the end terminus of the p6 was considered to be located at any point with a 12 nm radius of the C-terminus of the CA domain. Two dynamic frames were then simulated, and positions of Dendra2 molecules were analyzed statistically in a similar method to time-lapse iPALM sections. The images of the Dendra2 positions from these simulations do not show any major lattice dynamics, as presented in Fig. S8. The corresponding *p*-values for sections of the lattice in these simulations ranged between 0.66 and 0.97. The *p*-values from 0.66 to 0.97 are similar to the *p*-values observed for the fixed lattice. Although we cannot rule out the possibility of large flexible motions of NC and p6, our calculations demonstrate that this flexibility would not have a major impact on the observed Dendra2 dynamics within the immobilized Gag-Dendra2 VLPs.

Biochemical verification of Gag lattice dynamics

If Gag lattice dynamics exist, they should have biochemical manifestations, which we should be able to probe independently of fluorescence methods. HaXS8 is a membrane-permeable linker that creates a covalent bond between SNAP and Halo molecules (39,40). If lattice dynamics exist within the Gag VLPs, then SNAP and Halo molecules incorporated within the lattice of HIV Gag can be cross-linked with HaXS8 with a predictable concentration dependence and time dependence governed by dynamics of Gag-SNAP and Gag-Halo molecules within the lattice of individual VLPs.

To test this, we harvested VLPs assembled by 80% Gag plus 10% Gag-SNAP plus 10% Gag-Halo. When these VLPs are subjected to HaXS8 at different concentrations, the percentage of dimerization of the SNAP- and Halo-tagged Gag changed and peaked at a 1-μM concentration of HaXS8, as shown in Fig. 6 *A*. For a very high concentration of HaXS8, the percentage of dimerization is very low, which is not expected for a completely static lattice. However, because a SNAP-HaXS8 would not be able to bind Halo-HaXS8, the low dimerization at high HaXS8 concentrations suggests that at any given moment SNAP and Halo molecules are significantly distant within the Gag lattice. We went further to analyze the effect of incubation time on the dimerization. The VLPs were treated with 1 μM HaXS8 and incubated for time periods up to 90 min, as shown in Fig. 6 *B*. The data presented in Fig. 6 *B* show that the SNAP-HaXS8-Halo reaction is not instantaneous, and the amount of dimerization increases with an increase in time until it reaches saturation. The dynamics of SNAP-HaXS8-Halo in our study is by an order of magnitude slower than the one reported by Erhart et al., in which they used similar conditions to probe for diffusion of proteins in the cytosol (39). The timescales of dimerization with HaXS8 are consistent with the timescales of morphological changes we observed with iPALM and would be consistent with diffusion of SNAP- and Halo-tagged Gag within the Gag VLP limited by lattice dynamics.

DISCUSSION

Based on our characterization of Dendra2 photophysics, we have measured Gag-Dendra2 VLPs with 1400–2400 Gag-Dendra2 molecules within each VLP. These numbers are

molecular counts in individual VLPs and demonstrate a wide range of Gag-Dendra2 incorporation with various VLPs. The spread of our measurements, which is significantly large, cannot be justified by the propagation of errors in the photoswitching of Dendra2. Based on a 60% probability of photoswitching, we estimate that the error in counting 2000 molecules would be $\sqrt{2000 * (0.6)(0.4)} = 22$, which is significantly smaller than the spread of our calculated distribution. We therefore conclude that there is a large variation in the amount of filling observed in individual VLPs. Our measurements, both in terms of the average number of Gag molecules as well as the variety of defect sizes, are consistent with the electron cryotomography data (5). Our measurements are also in agreement with previously reported PCH analysis of VLPs, in which expression of fluorescently labeled Gag yielded between 800 and 2500 copies of Gag incorporated within VLPs (3).

Our high-resolution iPALM imaging of the Gag-Dendra2 VLPs, however, provides useful complementary information to the cryotomography data, mainly by exploring the dynamics within structures. Super-resolution techniques have been previously applied to study the assembly of HIV Gag virions (31,41); here, we have extended these techniques to investigate the morphology of the HIV Gag lattice and its fate over time after budding. The LCA, as presented in this manuscript, is heavily influenced by fluorescence correlation spectroscopy, which is a powerful tool to study diffusion, flow dynamics, and chemical reactions (42–47). Specifically, we utilized a multi-τ correlation analysis, which has advantages in exploring a wide range of delay times (48) with optimized computational power. The LCA developed here has the potential to uncover structural dynamics based on the localization information within a particular volume. We also estimated the effect of presumed structural flexibility of NC and p6 on our observed dynamics. A theoretical model was developed in which we considered the CA positions as static and estimated the effects of NC and p6 structural flexibility on dynamics of Dendra2 molecules. The statistical analysis (detailed in the Supporting Materials and Methods) reveals that the dynamics recorded by time-lapse iPALM cannot be explained by presumed structural flexibility of NC and p6 domains.

There are significant limitations to the LCA, as presented in our manuscript. Specifically, the decay in the correlation function is a convolution of photobleaching and structural dynamics within the analyzed volumes. For the purposes of the LCA, if each section of the structure were to contain an infinite supply of single molecules, then the LCA would have reported only on the structural dynamics. This is a shortcoming that can be overcome for structures with open interfaces to the buffer, where new molecules can bind into the structure from the buffer.

We also demonstrate the effects of lattice dynamics using cross-linking reaction between SNAP and Halo proteins embedded within the lattice of Gag VLPs. The heterodimerizer HaXS8 is membrane permeable and covalently cross-links to SNAP and Halo proteins (39,40). HaXS8 has been used to cross-link freely diffusing SNAP and Halo proteins within the cytoplasm (39). In the case of free diffusion of SNAP and Halo within the cytosol, cross-linking reached a saturated limit of ~60% efficiency within 10 min of application of HaXS8. Our experiments, as shown in Fig. 6, also reach 60% efficiency; however, the reactions are considerably slower, consistent with slow diffusion within the Gag lattice. This is well expected because the SNAP and Halo-tagged Gag in this case are diffusing within a spherical lattice within the VLP. The combination of cross-linking and fluorescence measurements demonstrate a wide range of diffusion rates within the lattice of HIV Gag VLPs. The mechanism of this diffusive process remains to be further studied in detail.

It is plausible that lattice dynamics within the immature lattice of the fully infectious virions can play a role in the initial protease dimerization and consequently its activation. In our studies, however, we have only observed dynamics within Gag-Dendra2 VLPs, which do not undergo maturation and, most importantly, do not incorporate the full HIV genome and Gag-Pol. The binding of the HIV genome to the NC domains of Gag may further restrain the dynamics of the Gag lattice. Further studies within the immature lattice of the fully infectious virions should be able to further shed light on these mechanisms. The dynamics within the Gag lattice are also likely influenced by the interactions within CA domains within the immature lattice. The CA domain interactions are important for stabilization of the conical capsid core (49–52), as well as the assembly and morphology of the virions (53–55). The effects of these interactions on the observed dynamics of the lattice will remain an open question that can be answered by future experiments.

CONCLUSION

Our study outlines the development of an assay to study morphological changes within structures as small as 120–160 nm. This method can potentially be applied to study the fate of HIV after budding. It can shed light on the mechanism of maturation, which has been difficult to investigate because of a lack of appropriate tools.

SUPPORTING MATERIAL

Supporting Material can be found online at https://doi.org/10.1016/j.bpj.2020.06.023.

AUTHOR CONTRIBUTIONS

I.S. and S.S. designed the experiments. S.S. prepared samples and designed the molecular biology products. I.S. performed iPALM and biochemical experiments and analyzed data. I.S. and S.S. wrote the manuscript.

ACKNOWLEDGMENTS

The authors thank Linda Nikolova for sample preparation and electron microscopy analysis and Rainer Daum for fruitful discussions related to the instrument.

This study was supported by National Institutes of Health Grant R01 AI150474 to (S.S.).

REFERENCES

1. Briggs, J. A. G., M. C. Johnson, …, V. M. Vogt. 2006. Cryo-electron microscopy reveals conserved and divergent features of gag packing in immature particles of Rous sarcoma virus and human immunodeficiency virus. *J. Mol. Biol.* 355:157–168.
2. Briggs, J. A. G., M. N. Simon, …, M. C. Johnson. 2004. The stoichiometry of Gag protein in HIV-1. *Nat. Struct. Mol. Biol.* 11:672–675.
3. Chen, Y., B. Wu, …, J. D. Mueller. 2009. Fluorescence fluctuation spectroscopy on viral-like particles reveals variable gag stoichiometry. *Biophys. J.* 96:1961–1969.
4. Carlson, L.-A., J. A. G. Briggs, …, H.-G. Kräusslich. 2008. Three-dimensional analysis of budding sites and released virus suggests a revised model for HIV-1 morphogenesis. *Cell Host Microbe*. 4:592–599.
5. Briggs, J. A. G., J. D. Riches, …, H.-G. Kräusslich. 2009. Structure and assembly of immature HIV. *Proc. Natl. Acad. Sci. USA*. 106:11090–11095.
6. Schur, F. K. M., W. J. H. Hagen, …, J. A. G. Briggs. 2015. Structure of the immature HIV-1 capsid in intact virus particles at 8.8 Å resolution. *Nature*. 517:505–508.
7. Sundquist, W. I., and H.-G. Kräusslich. 2012. HIV-1 assembly, budding, and maturation. *Cold Spring Harb. Perspect. Med.* 2:a006924.
8. Gheysen, D., E. Jacobs, …, M. De Wilde. 1989. Assembly and release of HIV-1 precursor Pr55gag virus-like particles from recombinant baculovirus-infected insect cells. *Cell.* 59:103–112.
9. Lee, S.-K., M. Potempa, and R. Swanstrom. 2012. The choreography of HIV-1 proteolytic processing and virion assembly. *J. Biol. Chem.* 287:40867–40874.
10. Bendjennat, M., and S. Saffarian. 2016. The race against protease activation defines the role of ESCRTs in HIV budding. *PLoS Pathog.* 12:e1005657.
11. Konvalinka, J., H.-G. Kräusslich, and B. Müller. 2015. Retroviral proteases and their roles in virion maturation. *Virology.* 479–480:403–417.
12. Chen, Y., J. D. Müller, …, E. Gratton. 1999. The photon counting histogram in fluorescence fluctuation spectroscopy. *Biophys. J.* 77:553–567.
13. Chen, Y., J. D. Müller, …, E. Gratton. 2002. Molecular brightness characterization of EGFP in vivo by fluorescence fluctuation spectroscopy. *Biophys. J.* 82:133–144.
14. Cocucci, E., F. Aguet, …, T. Kirchhausen. 2012. The first five seconds in the life of a Clathrin-coated pit. *Cell.* 150:495–507.
15. Böcking, T., F. Aguet, …, T. Kirchhausen. 2011. Single-molecule analysis of a molecular disassemblase reveals the mechanism of Hsc70-driven clathrin uncoating. *Nat. Struct. Mol. Biol.* 18:295–301.
16. Ulbrich, M. H., and E. Y. Isacoff. 2007. Subunit counting in membrane-bound proteins. *Nat. Methods.* 4:319–321.
17. Taniguchi, Y., P. J. Choi, …, X. S. Xie. 2010. Quantifying E. coli proteome and transcriptome with single-molecule sensitivity in single cells. *Science.* 329:533–538.
18. Greenfield, D., A. L. McEvoy, …, J. Liphardt. 2009. Self-organization of the *Escherichia coli* chemotaxis network imaged with super-resolution light microscopy. *PLoS Biol.* 7:e1000137.
19. Annibale, P., S. Vanni, …, A. Radenovic. 2011. Identification of clustering artifacts in photoactivated localization microscopy. *Nat. Methods.* 8:527–528.
20. Rollins, G. C., J. Y. Shin, …, S. Pressé. 2015. Stochastic approach to the molecular counting problem in superresolution microscopy. *Proc. Natl. Acad. Sci. USA*. 112:E110–E118.
21. Lee, S.-H., J. Y. Shin, …, C. Bustamante. 2012. Counting single photoactivatable fluorescent molecules by photoactivated localization microscopy (PALM). *Proc. Natl. Acad. Sci. USA*. 109:17436–17441.
22. Sydor, A. M., K. J. Czymmek, …, V. Mennella. 2015. Super-resolution microscopy: from single molecules to supramolecular assemblies. *Trends Cell Biol.* 25:730–748.
23. Kaksonen, M., and D. G. Drubin. 2006. PALM reading: seeing the future of cell biology at higher resolution. *Dev. Cell.* 11:438–439.
24. Hess, S. T., T. P. K. Girirajan, and M. D. Mason. 2006. Ultra-high resolution imaging by fluorescence photoactivation localization microscopy. *Biophys. J.* 91:4258–4272.
25. Rust, M. J., M. Bates, and X. Zhuang. 2006. Sub-diffraction-limit imaging by stochastic optical reconstruction microscopy (STORM). *Nat. Methods.* 3:793–795.
26. Shtengel, G., J. A. Galbraith, …, H. F. Hess. 2009. Interferometric fluorescent super-resolution microscopy resolves 3D cellular ultrastructure. *Proc. Natl. Acad. Sci. USA*. 106:3125–3130.
27. Fiolka, R., L. Shao, …, M. G. L. Gustafsson. 2012. Time-lapse two-color 3D imaging of live cells with doubled resolution using structured illumination. *Proc. Natl. Acad. Sci. USA*. 109:5311–5315.
28. Niu, L., and J. Yu. 2008. Investigating intracellular dynamics of FtsZ cytoskeleton with photoactivation single-molecule tracking. *Biophys. J.* 95:2009–2016.
29. Ishitsuka, Y., N. Savage, …, N. Takeshita. 2015. Superresolution microscopy reveals a dynamic picture of cell polarity maintenance during directional growth. *Sci. Adv.* 1:e1500947.
30. Biteen, J. S., M. A. Thompson, …, W. E. Moerner. 2008. Super-resolution imaging in live *Caulobacter crescentus* cells using photoswitchable EYFP. *Nat. Methods.* 5:947–949.
31. Floderer, C., J.-B. Masson, …, D. Muriaux. 2018. Single molecule localisation microscopy reveals how HIV-1 Gag proteins sense membrane virus assembly sites in living host CD4 T cells. *Sci. Rep.* 8:16283.
32. Bleck, M., M. S. Itano, …, S. M. Simon. 2014. Temporal and spatial organization of ESCRT protein recruitment during HIV-1 budding. *Proc. Natl. Acad. Sci. USA*. 111:12211–12216.
33. Prescher, J., V. Baumgärtel, …, D. C. Lamb. 2015. Super-resolution imaging of ESCRT-proteins at HIV-1 assembly sites. *PLoS Pathog.* 11:e1004677.
34. Van Engelenburg, S. B., G. Shtengel, …, J. Lippincott-Schwartz. 2014. Distribution of ESCRT machinery at HIV assembly sites reveals virus scaffolding of ESCRT subunits. *Science.* 343:653–656.
35. Pedersen, M., S. Jamali, …, S. Saffarian. 2019. Correlative iPALM and SEM resolves virus cavity and Gag lattice defects in HIV virions. *Eur. Biophys. J.* 48:15–23.
36. Lim, K. H., H. Huang, …, S. Park. 2013. Stable, high-affinity streptavidin monomer for protein labeling and monovalent biotin detection. *Biotechnol. Bioeng.* 110:57–67.
37. Saha, I., and S. Saffarian. 2019. Interferometric fluorescence cross correlation spectroscopy. *PLoS One.* 14:e0225797.
38. Chudakov, D. M., S. Lukyanov, and K. A. Lukyanov. 2007. Tracking intracellular protein movements using photoswitchable fluorescent proteins PS-CFP2 and Dendra2. *Nat. Protoc.* 2:2024–2032.
39. Erhart, D., M. Zimmermann, …, M. P. Wymann. 2013. Chemical development of intracellular protein heterodimerizers. *Chem. Biol.* 20:549–557.
40. Zimmermann, M., R. Cal, …, M. P. Wymann. 2014. Cell-permeant and photocleavable chemical inducer of dimerization. *Angew. Chem. Int.Engl.* 53:4717–4720.
41. Gunzenhäuser, J., N. Olivier, …, S. Manley. 2012. Quantitative super-resolution imaging reveals protein stoichiometry and nanoscale morphology of assembling HIV-Gag virions. *Nano Lett.* 12:4705–4710.

42. Magde, D., E. L. Elson, and W. W. Webb. 1974. Fluorescence correlation spectroscopy. II. An experimental realization. *Biopolymers.* 13:29–61.

43. Saffarian, S., H. Qian, …, G. Goldberg. 2006. Powering a burnt bridges Brownian ratchet: a model for an extracellular motor driven by proteolysis of collagen. *Phys. Rev. E Stat. Nonlin. Soft Matter Phys.* 73:041909.

44. Qian, H., and E. L. Elson. 2004. Fluorescence correlation spectroscopy with high-order and dual-color correlation to probe nonequilibrium steady states. *Proc. Natl. Acad. Sci. USA.* 101:2828–2833.

45. Saffarian, S., and E. L. Elson. 2003. Statistical analysis of fluorescence correlation spectroscopy: the standard deviation and bias. *Biophys. J.* 84:2030–2042.

46. Qian, H., S. Saffarian, and E. L. Elson. 2002. Concentration fluctuations in a mesoscopic oscillating chemical reaction system. *Proc. Natl. Acad. Sci. USA.* 99:10376–10381.

47. Chattopadhyay, K., S. Saffarian, …, C. Frieden. 2002. Measurement of microsecond dynamic motion in the intestinal fatty acid binding protein by using fluorescence correlation spectroscopy. *Proc. Natl. Acad. Sci. USA.* 99:14171–14176.

48. Wohland, T., R. Rigler, and H. Vogel. 2001. The standard deviation in fluorescence correlation spectroscopy. *Biophys. J.* 80:2987–2999.

49. Briggs, J. A. G., T. Wilk, …, S. D. Fuller. 2003. Structural organization of authentic, mature HIV-1 virions and cores. *EMBO J.* 22:1707–1715.

50. Gres, A. T., K. A. Kirby, …, S. G. Sarafianos. 2015. Structural virology. X-ray crystal structures of native HIV-1 capsid protein reveal conformational variability. *Science.* 349:99–103.

51. Wagner, J. M., K. K. Zadrozny, …, O. Pornillos. 2016. Crystal structure of an HIV assembly and maturation switch. *eLife.* 5:e17063.

52. Pornillos, O., B. K. Ganser-Pornillos, and M. Yeager. 2011. Atomic-level modelling of the HIV capsid. *Nature.* 469:424–427.

53. Ako-Adjei, D., M. C. Johnson, and V. M. Vogt. 2005. The retroviral capsid domain dictates virion size, morphology, and coassembly of gag into virus-like particles. *J. Virol.* 79:13463–13472.

54. Mammano, F., A. Ohagen, …, H. G. Göttlinger. 1994. Role of the major homology region of human immunodeficiency virus type 1 in virion morphogenesis. *J. Virol.* 68:4927–4936.

55. Accola, M. A., S. Höglund, and H. G. Göttlinger. 1998. A putative α-helical structure which overlaps the capsid-p2 boundary in the human immunodeficiency virus type 1 Gag precursor is crucial for viral particle assembly. *J. Virol.* 72:2072–2078.